fairly accurate polaron self-energies, and which yields a Fröhlich effective mass, closely simulating the Feynman-Schultz effective-mass approximation.

An alternative approach to obtaining the polaron effective mass is provided by a study of the cyclotron motion of a polaron which is discussed in the sequel to this paper.

ACKNOWLEDGMENT

Acknowledgment is made here to the Louisiana State University Computer Research Center for use of its IBM 360/65 computer for performing the numerical calculations.

---

[1] H. Fröhlich, Advan. Phys. 3, 325 (1954).

[2] T. D. Lee, F. E. Low, and D. Pines, Phys. Rev. 90, 297 (1953).

[3] L. Landau, Phys. Z. Sowjetunion 3, 664 (1933).

[4] S. I. Pekar, J. Phys. USSR 10, 341 (1946).

[5] E. H. Lieb and K. Yamazaki, Phys. Rev. 111, 728 (1958).

[6] R. P. Feynman, Phys. Rev. 97, 660 (1955).

[7] T. D. Schultz, Phys. Rev. 116, 526 (1959).

[8] G. Höhler, Z. Naturforsch. 9A, 801 (1954).

[9] G. R. Allcock, Advan. Phys. 5, 413 (1956).

[10] B. U. Stewart, Ph. D. thesis, Louisiana State University, 1971 (unpublished).

PHYSICAL REVIEW B VOLUME 2, NUMBER 10 15 NOVEMBER 1970

Spin Exchange in Excitons, the Quasicubic Model and Deformation Potentials in II-VI Compounds

D. W. Langer and R. N. Euwema
Aerospace Research Laboratories, Wright-Patterson Air Force Base, Ohio 45433

and

Koh Era* and Takao Koda†
Ohio State University, Columbus, Ohio 43210

(Received 11 May 1970)

The effect of the spin-exchange interaction between electron and hole is investigated for the case of excitons originating from one of the p-like valence bands and an s-like conduction band, as is the case for IIb-VIb compounds. A general exciton matrix is constructed, starting from the work of Pikus. It includes spin-orbit, crystal-field, spin-exchange, and deformation-potential interactions. Use of this matrix then allows a theoretical fit to our experimental data which describes the shift of exciton levels under uniaxial pressure in ZnO, CdS, and CdSe. This fit results in the determination of six deformation potentials, two spin-orbit parameters, the crystal-field parameter, and the exchange parameter. The general theory, when adapted to the zinc-blende structure, allows us to fit our data on cubic ZnS and ZnSe, resulting in a determination of two deformation potentials and the spin-exchange parameter for each compound.

I. INTRODUCTION

The phenomenon of free excitons in semiconducting crystals has been a subject of considerable interest for many years and has been summarized in general by Knox,[1] and in particular with respect to group II-VI compounds by Reynolds *et al.*[2] It has always been clear that the exciton properties are closely related to the fundamental properties of the materials in which they were observed. For the interpretation of these exciton spectra, one usually considers that an exciton is composed of two particles: an electron in a conduction band and a hole in a valence band which are bound together by the Coulombic interaction. It is customarily assumed further that the j-j coupling scheme holds for these exciton states in the framework of the one-electron energy-band model. Thus, multiple structures in the exciton spectra are attributed to the excitonic transitions arising from the split-off valence bands. One usually equates the energy difference between two excitons in a cubic material such as zinc-blende ZnS with the spin-orbit splitting of its valence band. In wurtzite CdS, Hopfield related the observed energy differences of the three free excitons observed near the fundamental gap to the spin-orbit and crystal-field parameters of the CdS valence band on the basis of the quasicubic model.[3] This procedure has been generally followed in the interpretation of the valence-band splitting of other wurtzite II-VI compounds.[4]

Measurements of the stress-induced energy shifts of the exciton lines on CdTe,[5] CdSe,[6] ZnTe,[7] CdS,[8] and ZnO[9] were related to the change of the energy separations, effective masses, and the degeneracies of the relevant energy bands, and the results were interpreted in terms of the usual deformation potential theory as initially given by Kleiner and Roth.[10]

Experimental evidence that such an approximation may be quite inappropriate has been found during the course of uniaxial stress measurements on the wurtzite type II-VI compounds. As has been reported in a previous paper,[11] there occurs a quite remarkable splitting of the exciton lines under a particular geometry of the stress with respect to the crystallographic axes. Since in the wurtzite crystal all of the orbital degeneracies of the valence band are lifted by the combined effect of the trigonal crystal field and the spin-orbit interaction, the observed splitting of the exciton lines could not be accounted for by the usual deformation-potential theory based on the one-electron energy-band scheme. We had suggested that the observed stress-induced splitting should be attributed to the decomposition of the degenerate Γ_5 exciton state by the deformation of the wurtzite lattice. Consequently, we have to deal with this problem by explicitly taking account of the symmetry of the exciton states including the electron and hole spins.

Subsequently, this interpretation has been given a theoretical foundation by Akimoto and Hasegawa.[12] They investigated the combined effects of stress and the electron-hole exchange interaction in a quasicubic model and were able to predict the splitting and polarization pattern of the Γ_5 exciton we had found experimentally. The authors pointed out that it is combined effects of stress and exchange coupling which cause the splitting. If either one is zero, the splitting of the Γ_5 exciton is zero. Thus, the importance of the spin exchange is demonstrated and, in general, the inclusion of it bridges the description of the excitons in the j-j coupling scheme with the description in the L-S coupling scheme, with an increasing value of the exchange parameter.[1]

In this paper, we generalize the theory to include the exciton properties at the Γ point in hexagonal and in cubic crystals, and we use it to analyze our measurements of the stress-induced energy shift of the exciton reflectivity structure of ZnO, CdS, CdSe, ZnS, and ZnSe. Preliminary results were reported earlier.[13]

Our main concern is to establish the spin-exchange constants for excitons in II-VI compounds. The analysis of our experimental data, however, furnishes us at the same time with quantitative values for the spin-orbit, crystal-field, and deformation-potential parameters. It then is also possible to compare our spin-orbit values for ZnO, CdS, and CdSe with those derived via the quasicubic approximation and thus to evaluate for the first time the applicability of the quasicubic model for different hexagonal compounds.

The cubic crystals of ZnS and ZnSe also show a stress-induced splitting of the A exciton at the Γ point. This is different from the case for hexagonal crystals because the top valence bands and corresponding exciton states are still degenerate if one neglects the exchange interaction. The effect of the stress-exchange coupling becomes evident in our experiments by an increase of the intensity of the corresponding forbidden exciton transition. At other symmetry points of cubic crystals, the valence bands are nondegenerate and splittings due to stress-induced exchange coupling may be observed. For example, Rowe, Pollak, and Cardona[14] demonstrated the existence of hyperbolic excitons in GaAs with the help of the stress-induced exchange splitting.

In the following sections, we will outline the experimental procedures and the experimental results. Thereafter, in Sec. IV, a theoretical treatment is presented for the exciton states with the inclusion of deformation, spin-orbit, and spin-exchange coupling for hexagonal and cubic crystals. In Sec. V, the experimental results are summarized and compared with a parameter fit of the theory. The resulting parameters are discussed. As additional supporting evidence, predictions on the basis of this fit concerning intensity variations of exciton lines with pressure are compared with experiment.

II. EXPERIMENTAL PROCEDURES

Reflection spectra were recorded at near normal incidence on uniaxially stressed samples of ZnO, CdS, and CdSe with wurtzite structure and on samples of ZnS and ZnSe with zinc-blende structure in the wavelength region near the respective absorption edge of each sample.

A. Stress Apparatus and Samples

Among several experimental difficulties which we encountered in performing stress measurements, the most serious one is the rather poor reproducibility of the results for every experimental run. This is mainly due to the nonuniform stress distribution within the sample. In order to minimize this effect, we employed a hydraulic pressure system which is capable of a continuous loading of uniaxial force up to about 4 ton. The

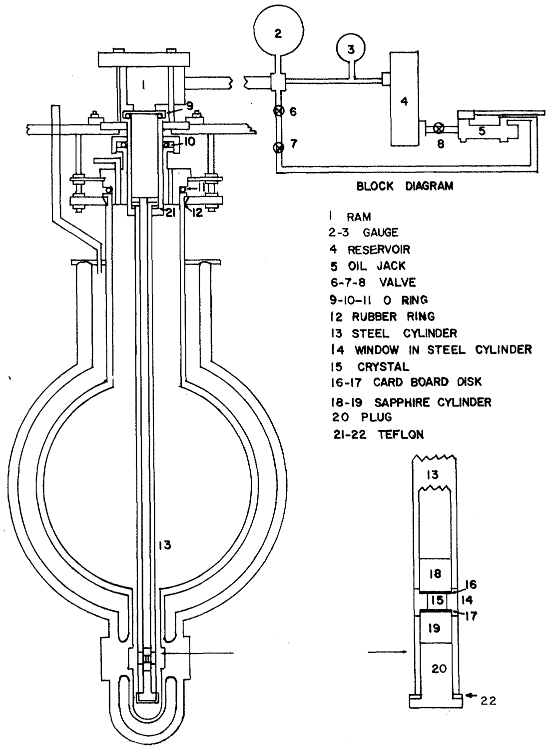

FIG. 1. Hydraulic pressure system and uniaxial stress apparatus.

details of the pressure system are shown in Fig. 1.

In this figure, an oil jack (5) produces a hydraulic pressure up to about 10^4 psi in the oil contained in a reservoir (4). The reservoir has a sufficient volume to maintain the pressure at a particular load during the photographic measurements of the reflection spectra. The pressure of the oil is directly measured by a calibrated Heise Bourdon gauge (2). The unidirectional pressure on the sample is generated by a ram (1) which exerts a force onto a sample through a long stainless-steel piston-cylinder arrangement (13) inside a glass Dewar. An oriented sample (15) with a parallelepiped shape is mounted between two sapphire cylinders (18, 19) having optically polished surfaces. Small cardboard discs were successfully used at both interfaces between the sapphire cylinders and the sample to minimize the nonuniform distribution of stress. The sapphire cylinders and the sample are mounted at the bottom end of a stainless-steel cylinder where small openings are provided for the optical measurements. All measurements were made at about 1.8 °K with the sample immersed in liquid helium pumped to below the λ point.

Samples were cut from blocks of single crystals. We used hexagonal (wurtzite) ZnO, grown by a hydrothermal method at Airtron, a division of Litton Industries, and hexagonal CdS and CdSe, both grown from the vapor phase at the Aerospace Research Laboratories. The samples were cleaved or cut and polished into parallelepipeds with mutually perpendicular surfaces of $(11\bar{2}0)$, $(1\bar{1}00)$, and (0001). The size of the samples is about $5\times5\times4$ mm.[3] The reflection measurements were made on $(1\bar{1}00)$ cleavage planes or on (0001) planes. The latter planes mostly originated from natural grown surfaces treated with a suitable chemical etching solution.

Samples of ZnS and ZnSe were cut from larger single crystals grown from the melt by the Eagle-Picher Co. X-ray Laue patterns confirmed the cubic (zinc-blende) structure of the ZnSe crystals, though twinning planes, normal to the [111] direction could be optically observed in nearly all samples. The x-ray patterns showed that our melt-grown ZnS crystals were not as completely cubic as were the ZnSe crystals. Ebina and Takahashi and Anan'eva *et al.*[15] studied melt-grown ZnS and described it as cubic with many stacking faults of microscopic order normal to the [111] direction, exhibiting an x-ray pattern similar to an hexagonal crystal with a "*c* axis" along the [111] direction. Our crystals were of the same nature.

B. Optical Measurements

Reflection spectra were measured during the uniaxial compression of the sample. Light from a 100-W xenon discharge lamp was focused on a side surface of the sample with the angle of incidence to the normal of the face being smaller than 5°. The reflected light was led to a 2-m Bausch & Lomb grating spectrograph having an inverse dispersion of 0.4 nm/mm. The *k* vector of the incident light was always perpendicular to the direction of the uniaxial stress $\vec{P}$ applied to the sample. The reflection spectra were measured for light polarized with the electric vector $\vec{E}$ parallel or perpendicular to the applied stress $\vec{P}$ by using a Glan-Thompson prism or film polarizer placed in front of the entrance slit of the spectrograph. (These polarizations are referred to hereafter as $\vec{E}\parallel\vec{P}$ and $\vec{E}\perp\vec{P}$, respectively.) The geometries of the reflection measurements under uniaxial stress are thus determined by the relative orientations of the applied stress with respect to the particular crystallographic axis of the sample and with respect to the electric vector of the light. Different geometries employed in the present measurement for the hexagonal crystals are illustrated in Fig. 2. Measurements were also made in a geometry where *P* was 45° to the *c* axis for the hexagonal crystals.

In each experimental run, the reflection spectra were photographed during each stepwise increase of the stress for both polarizations $\vec{E}\parallel\vec{P}$ and $\vec{E}$

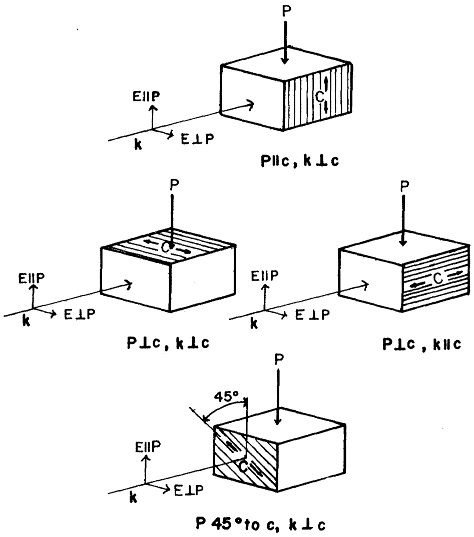

FIG. 2. Four experimental geometries of the reflection measurements on hexagonal crystal under uniaxial stress. Directions of the uniaxial stress *P*, the crystallographic *c* axis *c*, and the *k* vector and the electric vector *E* of the incident light are shown schematically.

$\perp \vec{P}$. After reaching the maximum load, usually at about 4 to 5 kbar, the pressure was completely released to zero. Usually the spectrum was found to return to the original zero-pressure shape to within the experimental accuracy. In cases where the spectra showed appreciable residual change, the data were omitted from further analysis. For each geometry, five to six samples were examined.

The few available ZnSe samples which were free of twinning were stressed along the axes $\vec{P} \parallel [110]$ and $\vec{P} \parallel [100]$. Crystals with twinning and stacking faults coplanar with the (111) planes were stressed in those directions in which the stress produced on both sides of the fault plane was identical, i.e., $\vec{P} \parallel [11\bar{2}]$ and $\vec{P} \parallel [111]$.

Besides these uniaxial compression measurements, the change in the reflection spectrum of thin platelets of ZnO crystal was measured during elastic bending. A ZnO platelet having a $(11\bar{2}0)$ surface was mounted on a four-point bending apparatus and was circularly bent around the *c* axis. The reflection spectra observed on the convex and concave sides were compared with the spectra of the unstrained surface. Since the surface on the convex side is elongated along the direction perpendicular to the bending axis, the result of these measurements was expected to give qualitative information on the spectral change for the uniaxial elongation perpendicular to the *c* axis. The experimental results are described in Sec. III.

III. EXPERIMENTAL RESULTS

The changes in the reflection spectra of ZnO are shown in Fig. 3 for the different experimental geometries. Three main reflection anomalies with the reflection minima at about 366.9 nm (3.379 eV) and 365.2 nm (3.395 eV) for $\vec{E} \perp c$ and at about 360.8 nm (3.436 eV) for $\vec{E} \parallel c$ at atmospheric pressure (0 kbar) correspond to the *A*, *B*, and *C* excitons, respectively, as denoted by Thomas.[16]

Minor structure appearing at about 357.2 nm (3.471 eV) corresponds to the *C'* exciton after Thomas's nomenclature.[16] The small peak at around 368.8 nm (3.362 eV) is due to an impurity emission line.

In the geometries other than the case of $\vec{P} \perp c$ and $\vec{k} \parallel c$, all exciton lines simply shift in energy without splitting, while in the case of $\vec{P} \perp c$, $\vec{k} \parallel c$, a quite remarkable splitting occurs in both the *A* and *B* excitons. As can be seen in Fig. 3, the split components are completely polarized with the electric vectors parallel and perpendicular to the stress direction. The polarization pattern for the *B* exciton is reversed as compared with that of the *A* exciton. In addition to this stress-induced splitting, we notice a remarkable intensity change in the split components. (This effect can also be accounted for theoretically by the combined effect of stress and spin exchange to be described later.)

In Fig. 4, we plot the shift and splitting of the *A*, *B*, *C*, and *C'* exciton lines against the applied stress for four samples, one for each stress direction. Instead of determining the accurate exciton resonance energies, experimental points were taken at the unique characteristic positions

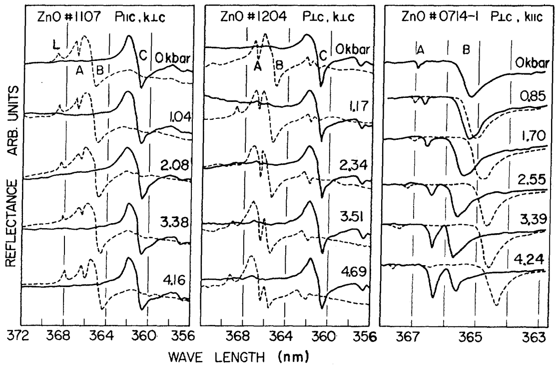

FIG. 3. Change of the reflection spectra of ZnO due to uniaxial stress at 1.8 °K. The solid line represents the polarized components with $\vec{E} \parallel \vec{P}$, the dashed line the ones with $\vec{E} \perp \vec{P}$. *A*, *B*, and *C* designate the reflection anomalies due to the respective excitons.

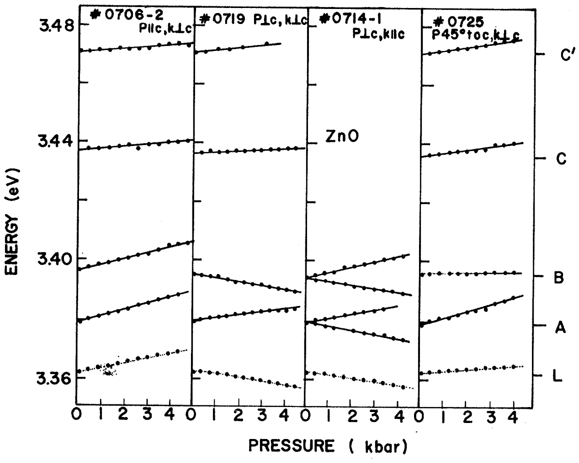

FIG. 4. Plot of the stress-induced shifts and splitting of exciton lines in ZnO at 1.8 °K. The experimental points were taken at reflection minima. Shift of the bound exciton emission lines are shown by dashed lines.

of the respective reflection anomalies, in most runs at their reflection minima. The energy positions of the observed exciton reflection minima at zero stress agreed well in all cases with the values published for the respective excitons. In the same figure, the shift of the impurity emission line is also shown by broken lines.

Occurrence of the stress-induced splitting of the A and B exciton lines can be observed only in the geometry $\vec{P}\perp c$, $\vec{k}\parallel c$. When the k vector of the incident light is perpendicular to the c axis, both lines seem to shift without splitting. However, they should actually be considered to be one of the components only of the split A and B lines. (Since the A and B lines are strongly polarized with $\vec{E}\perp c$, only the components with $\vec{E}\parallel\vec{P}$ can be observed in this geometry.) In fact, the energy shifts and the intensity change of these lines are exactly the same as those of the split components with $\vec{E}\parallel\vec{P}$ observed in the geometry $\vec{P}\perp c$, $\vec{k}\parallel c$.

As can be seen in Fig. 4, the shifts and splittings of the exciton lines in ZnO are nearly linear as a function of the applied compressive stress. Then, if the sign of the stress is reversed, that is, if we apply a uniaxial tensile stress, one would expect that the A and B excitons should split by the same amount but with the reversed polarization pattern. A qualitative verification of this was made by the bending experiment described before. Figure 5 shows the change of the reflection spectra observed at the convex and concave sides of a platelet ZnO crystal circularly bent around the c axis. On the concave side, the stress is compressive and perpendicular to the c axis. The spectral change is qualitatively similar to the corresponding spectra of the uniaxial compression under $\vec{P}\perp c$ and $\vec{k}\perp c$. In contrast, the observation on the convex side, where the lattice is elongated perpendicular to the c axis, shows the opposite; namely, the A line shifts to lower energy with decreasing intensity, while the B line shifts oppositely to higher energy with increasing intensity. These qualitative observations indicate that the splitting of the A and B lines under the tensile uniaxial stress occurs indeed with the reversed polarization pattern as expected.

The thin platelet ZnO crystal grown from the vapor phase has a more perfect lattice than the bulk ZnO crystals, and we can clearly observe structures ascribed to the higher excited states of the A and B excitons on the high-energy side of the B line.[16] As seen in Fig. 5, these structures also show stress-dependent changes. The intensity of a double structure marked as A' and A'' follows that of the A line, while structures B' and B'' follow the B line in intensity, indicating

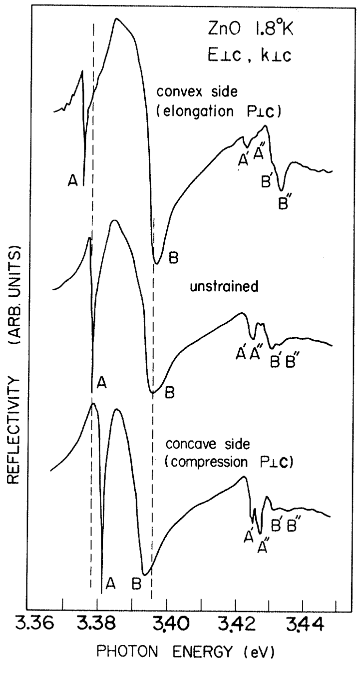

FIG. 5. Change of the reflection spectra of a ZnO platelet crystal in the bending experiment. The spectra observed on the convex (top) and the concave (bottom) sides of the $(2\bar{1}\bar{1}0)$ platelet surface are shown in comparison with the spectrum observed on the unstrained surface (middle). The bending axis is parallel to the c axis, and the polarization of the incident light is $\vec{E}\perp c$, $k\perp c$. The structures corresponding to the higher excited states of the A and B excitons are marked with A', A'' and B', B''.

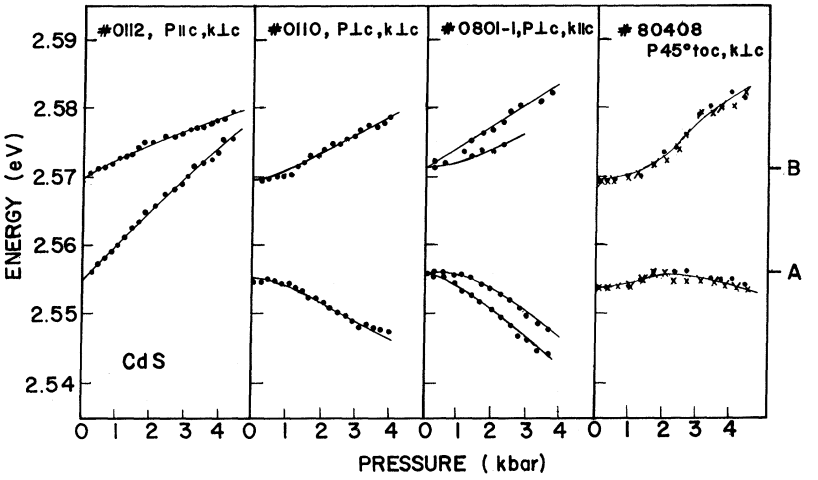

FIG. 6. Plot of the stress-induced shifts and splitting of the exciton lines in CdS at 1.8 °K.

that these double structures are associated with the respective ground-state excitons. Although no work has been attempted beyond such qualitative observations, a more detailed study in the future will be helpful in the study of excited states.

A. Results on CdS (Hexagonal)

The results of similar measurements on CdS are shown in Fig. 6. Again, the experimental points were taken at the minima of the respective reflection anomalies. The notations of the *A*, *B*, and *C* exciton lines follow the nomenclature of Thomas and Hopfield.[17] The stress-exchange splitting of the *A* and *B* excitons is observed in the same geometry $\vec{P}\perp c$, $\vec{k}\parallel c$, as in ZnO. Typical spectra showing this splitting are shown in Fig. 7. As can be seen in this figure, the qualitative features of the splitting are quite similar to the case of ZnO with respect to the polarization pattern and the intensity change of the split components. The magnitude of the splitting is, however, much smaller and both the *A* and *B* lines show nonlinear shifts and splittings, in contrast to the almost linear change in ZnO.

B. Results on CdSe (Hexagonal)

Figure 8 shows a similar plot for CdSe. The measurements of the stress-exchange splitting in CdSe were rather difficult, because the natural grown (0001) surfaces available for the $\vec{k}\parallel c$ measurements were quite small in area, and we were not successful in satisfactorily preparing good reflection surfaces by the mechanical polishing and the conventional chemical etching techniques. The measurements have been attempted on two natural (001) surfaces of sublimation grown crystals. The exciton energies were in good agreement with those reported for platelet-type crystals by Dimmock and Wheeler.[18] The *A* exciton line was found to split in both samples, as can be seen in Fig. 9. The polarization pattern is opposite to the case of ZnO and CdS in the sense that the higher-energy component is polarized with $\vec{E}\perp\vec{P}$. The *B* line was too broad to allow one to detect a

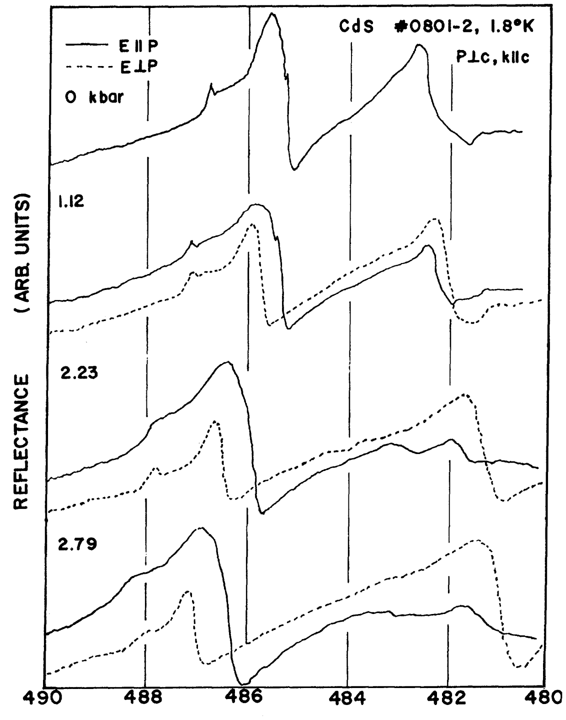

FIG. 7. Stress-exchange splitting of the $A(\Gamma_5)$ and $B(\Gamma_5)$ excitons in CdS in the geometry of $\vec{P}\perp c$, $\vec{k}\parallel c$. The solid and broken lines represent the polarized components with $\vec{E}\parallel\vec{P}$ and $\vec{E}\perp\vec{P}$, respectively.

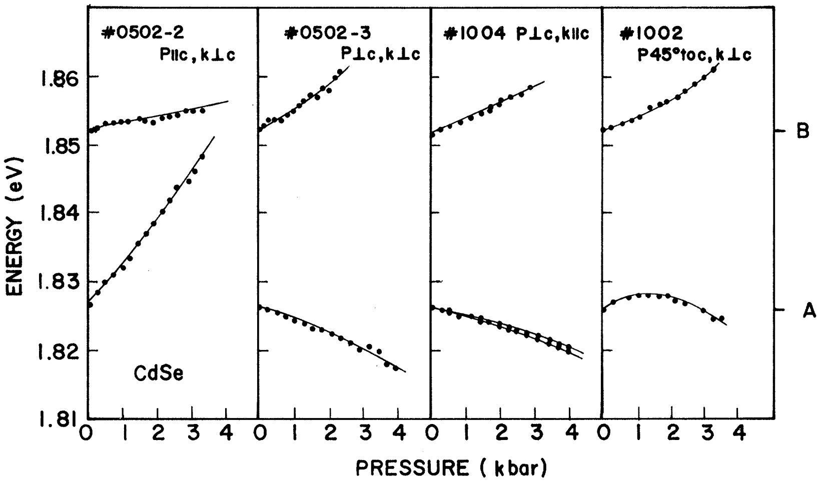

FIG. 8. Plot of the stress-induced shifts and splitting of the exciton lines in CdSe at 1.8 °K.

stress-dependent difference in the polarized components of the spectra.

C. Results on ZnSe (Cubic)

Most of the melt-grown ZnSe samples showed a number of macroscopic twinning boundaries parallel to the (111) plane. Stress was applied on such crystals in directions parallel and perpendicular to these boundaries $\vec{P} \parallel [11\bar{2}]$ and $\vec{P} \parallel [111]$ in order to minimize the effect of these imperfections.

The reflection spectra pertaining to the A exciton are shown in Fig. 10 for several pressure values and for the orientation of the pressure parallel to the [111] direction. The energy position of the exciton at atmospheric pressure agrees well with that reported by Hite *et al.*[19] The reflection spectra are, of course, unpolarized when axial pressure is not applied. However, when axial pressure is applied, depending on the orientations of the E vector with respect to the pressure direction, $\vec{E} \parallel \vec{P}$ or $\vec{E} \perp \vec{P}$, different spectra are observed. The $\vec{E} \parallel \vec{P}$ spectrum (solid line) remains nearly unchanged with pressure. The reflection spectrum in the $\vec{E} \perp \vec{P}$ polarization (dashed line) splits and shifts, and we notice a change of the intensity ratio between the two components: The low-energy component of $\vec{E} \perp \vec{P}$ appears only at pressures above 0.6 kbar. Then, with further increase in pressure up to about 2.5 kbar, it gains intensity in comparison with the high-energy $\vec{E} \perp \vec{P}$ component. At all pressures above 2.5 kbar, the ratio between the two components remains constant.

As an example of our measurements on several samples, the results obtained on two samples are plotted for $\vec{P} \parallel [11\bar{2}]$ and $\vec{P} \parallel [111]$ in Fig. 11. It is observed that the $A(\Gamma_5)$ exciton splits into two components. One, polarized $\vec{E} \perp \vec{P}$ and strongly pressure dependent, shifts to higher energies. One, $\vec{E} \parallel \vec{P}$, which is relatively pressure independent, shifts at higher pressures slightly toward lower energies. Furthermore, at pressures above 0.6 kbar, a third reflection structure, polarized $\vec{E} \perp \vec{P}$, appears at the low-energy side of the $\vec{E} \parallel \vec{P}$ branch. The energy dependence of this branch is relatively small. We will show that these observations are in qualitative agreement with the theory to be developed in Sec. IV.

Additionally, two measurements were made on fault-free samples with pressure parallel to either

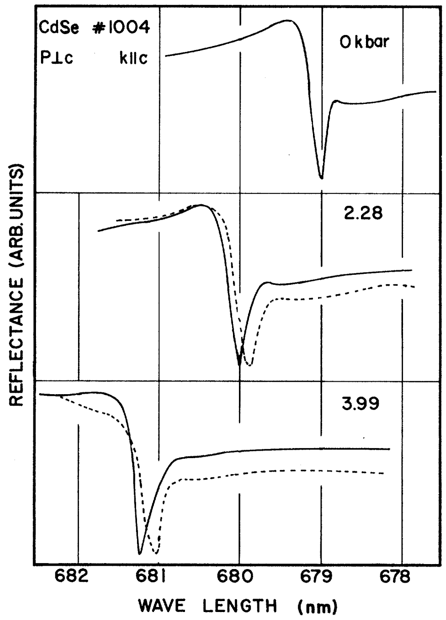

FIG. 9. Stress-exchange splitting of the $A(\Gamma_5)$ exciton in CdSe in the geometry of $\vec{P} \perp c$, $\vec{k} \parallel c$. The solid and broken lines represent the polarized components with $\vec{E} \parallel \vec{P}$ and $\vec{E} \perp \vec{P}$, respectively.

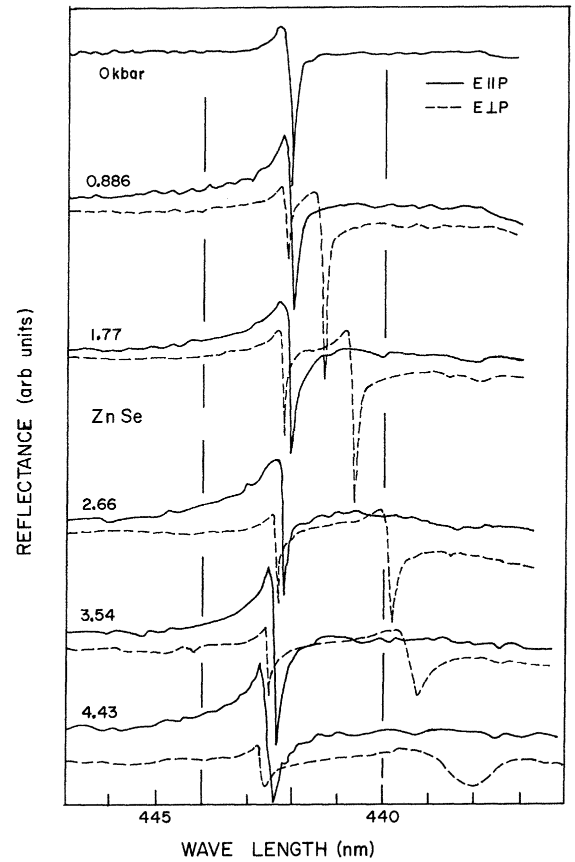

FIG. 10. Change of the reflection spectrum of the A exciton in ZnSe at 1.8 °K with uniaxial stress parallel to the [111] direction. Solid line denotes $\vec{E}$ vector parallel to the direction of pressure, $\vec{E}\parallel\vec{P}$, dashed line $\vec{E}\perp\vec{P}$.

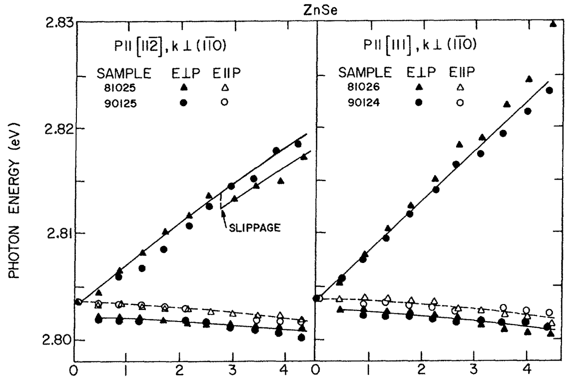

FIG. 11. Plot of the stress-induced change and splitting of the A exciton in ZnSe at 1.8 °K for two different samples each with $P\parallel[11\bar{2}]$ and [111]. Polarizations $\vec{E}\perp\vec{P}$ and $\vec{E}\parallel\vec{P}$ are indicated by closed and open points, respectively.

the [100] or the [110] axes. These results agree with the above within the framework of the following interpretations.

D. Results on ZnS (Cubic)

The optical reflection spectra of our ZnS samples were similar in shape and agreed as to the energy positions with those reported by Birman, Samelson, and Lempicki.^{20} The observed structure of the reflection spectra confirmed our assumption that the crystals were not hexagonal, but were indeed cubic.

The melt-grown samples of ZnS had many stacking faults parallel to the (111) plane. Consequently, stress was applied in the direction parallel and perpendicular to the normal of the fault planes, $\vec{P}\parallel[111]$ and $\vec{P}\parallel[11\bar{2}]$, in order to induce the same stress in all segments of the stack-faulted crystal. Internal stress probably caused by the faulting planes could, of course, not be eliminated. The ZnS crystals were of much less perfect structure than the ZnSe crystals, and the results for ZnS (Fig. 12) are, consequently, not as reliable as those for ZnSe. Still, one recognizes the same features in both ZnS and ZnSe. The $A(\Gamma_5)$ exciton splits into two components. One, $\vec{E}\perp\vec{P}$, shifts strongly to higher energies. One, $\vec{E}\parallel\vec{P}$, which is relatively pressure independent, shifts slightly to lower energies at higher pressures. Again a third component appears at higher stress, which is displaced approximately parallel to the $\vec{E}\perp\vec{P}$ component toward lower energies. In comparison with ZnSe, however, the lower energy $\vec{E}\perp\vec{P}$ branch in ZnS becomes observable only at 1.75 kbar. Its intensity seems to have leveled at 3 kbar. The separation from the $\vec{E}\parallel\vec{P}$ branch is several times that in ZnSe.

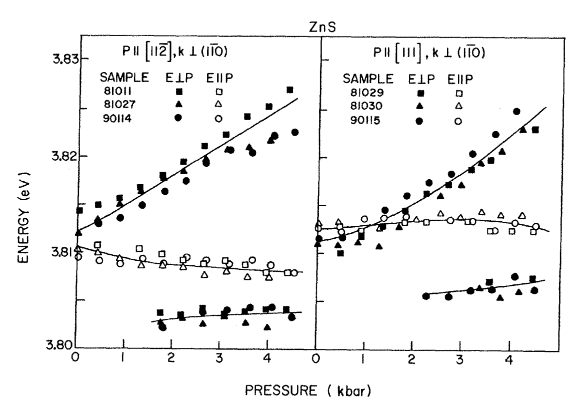

FIG. 12. Plot of the stress-induced change and splitting of the A exciton in ZnS at 1.8 °K for three different samples each with $\vec{P}\parallel[11\bar{2}]$ and $\vec{P}\parallel[111]$.

The results at low pressures (0 to 1.5 kbar) are less clear. The $\vec{E} \parallel \vec{P}$, and the upper $\vec{E} \perp \vec{P}$ components, do not seem to extrapolate to a single exciton position at atmospheric pressure: $\vec{P} \parallel [111]$ shows a crossing, while $\vec{P} \parallel [11\bar{2}]$ shows still a separation. We consider this to be the effect of the internal stress due to the faults, indicating an internal tension parallel to [111] and an internal compression perpendicular to it, i.e., parallel to the $[11\bar{2}]$ direction. Consequently, the applied pressure does not correspond exactly to the pressure causing the splitting and the deduced results for ZnS will not be as reliable as for the other crystals above. Nevertheless, we included this example because the results are sufficiently accurate to demonstrate the characteristic features of the spin-exchange effect.

IV. THEORY

The band structure of all the investigated compounds has been calculated by the pseudopotential,[21] self-consistent orthogonalized-plane-wave (OPW),[22] or Korringa-Kohn-Rostoker (KKR)[23] method, and are fairly well understood. They are all direct-band-gap semiconductors with the valence-band maximum and conduction-band minimum both occurring at the Γ point of the Brillouin zone. The Γ point structure of the important bands is shown in Fig. 13 for both the zinc-blende and wurtzite symmetries. The conduction band is *s*-like in character and is spin degenerate. The top three valence bands are *p*-like in character. They are split by the spin-orbit interaction, and in the case of wurtzite symmetry also by the crystal field. Excitons have been observed with the electron in the conduction band and the hole in each of the valence bands. The labeling of these excitons (*A*, *B*, and *C*) is indicated in Fig. 13.

The effective Hamiltonian formalism of Pikus[24] can be used to describe the exciton problem. The exciton Hamiltonian can be divided into the pieces

$$H = H_{v-0} + H_{v-p} + H_c + H_{\text{exciton}} ,$$

where H_{v-0} describes the zero-pressure mixing of the three *p*-like valence bands, H_{v-p} describes the strain-dependent mixing of the valence bands, H_c describes the conduction-band energy, and H_{exciton} describes the valence-hole–conduction-electron interaction. Each term will be discussed in detail. As can be seen from this Hamiltonian, we are assuming that the three valence bands are sufficiently far removed from other bands, that mixing with other bands can be neglected. Mixing of the conduction band with other bands is also neglected.

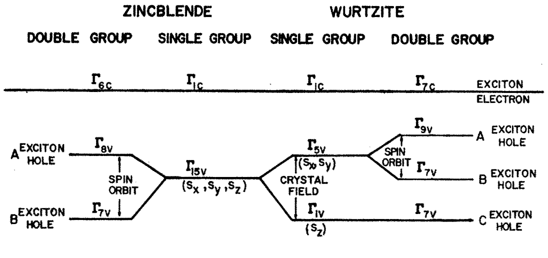

FIG. 13. Structure and symmetries of the lowest conduction and upmost valence bands in II-VI compounds at the Γ point.

The operator H_{v-0} describes the zero-pressure valence-band mixing. The *p*-like basis functions S_x, S_y, and S_z can be used, or more conveniently, one can use the set

$$S_+ = -(S_x + iS_y)/\sqrt{2}, \quad S_0 = S_z, \quad S_- = (S_x - iS_y)/\sqrt{2} .$$

Band mixing can be described in terms of the $L = 1$ angular momentum matrices

$$J_+ = (1/\sqrt{2})\,(J_x + iJ_y) = \begin{pmatrix} 0 & 1 & 0 \\ 0 & 0 & 1 \\ 0 & 0 & 0 \end{pmatrix} ,$$

$$J_0 = J_z = \begin{pmatrix} 1 & 0 & 0 \\ 0 & 0 & 0 \\ 0 & 0 & -1 \end{pmatrix} ,$$

$$J_- = (1/\sqrt{2})\,(J_x - iJ_y) = \begin{pmatrix} 0 & 0 & 0 \\ 1 & 0 & 0 \\ 0 & 1 & 0 \end{pmatrix} .$$

The familiar functions α and β can be used for a spin basis. The spin interaction can then be described by use of the Pauli-spin matrices. In terms of these operators, the zinc-blende valence-band interaction matrix can be written

$$H_{v-0}^{\text{ZB}} = \Delta J \cdot \sigma ,$$

where the operations J and σ operate on valence-electron wave functions. The resulting 6×6 matrix is labeled by the basis $S_+\alpha$, $S_+\beta$, $S_-\alpha$, $S_-\beta$, $S_0\alpha$, and $S_0\beta$. This matrix has four spin-$\frac{3}{2}$ eigenvalues with energy Δ, and two spin-$\frac{1}{2}$ eigenvalues with energy -2Δ. The total spin-orbit splitting is thus 3Δ (see Fig. 14). The comparable wurtzite operator according to Pikus is

$$H_{v-0}^{w} = \Delta_1 J_z^2 + \Delta_2 J_z \sigma_z + \Delta_3 (\sigma_+ J_- + \sigma_- J_+) .$$

The corresponding 6×6 matrix splits into two identical 3×3 matrices with bases $S_+\alpha$, $S_-\alpha$, $S_0\beta$, and $S_-\beta$, $S_+\beta$, $S_0\alpha$. The matrix is

$$\begin{pmatrix} \Delta_1 + \Delta_2 & 0 & 0 \\ 0 & \Delta_1 - \Delta_2 & \sqrt{2}\Delta_3 \\ 0 & \sqrt{2}\Delta_3 & 0 \end{pmatrix} .$$

The physical meaning of the coefficients Δ_1, Δ_2,

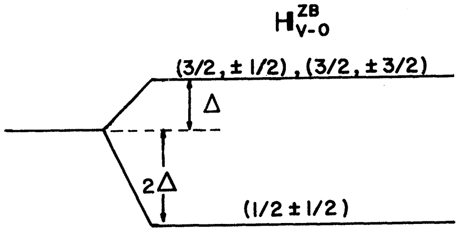

FIG. 14. Effect of the zinc-blende spin-orbit Hamiltonian $H^{\mathrm{ZB}}_{v\text{-}0}$ on the valence band.

and Δ_3 can be better understood on the basis of (i) a crystal field splitting of the S_x, S_y bands from the S_z band, (ii) a spin-orbit splitting of the $j=\frac{3}{2}$ bands from the $j=\frac{1}{2}$ band, and (iii) a trigonal splitting of the $(j,m)=(\frac{3}{2},\pm\frac{3}{2})$ bands from the $(\frac{3}{2},\pm\frac{1}{2})$ bands. This situation is summarized in Fig. 15. Using the relationships

$$S_+\alpha=(\tfrac{3}{2},\tfrac{3}{2}) ,$$

$$S_-\alpha=(\sqrt{3})^{-1}(\tfrac{3}{2},-\tfrac{1}{2})-(\sqrt{\tfrac{2}{3}})(\tfrac{1}{2},-\tfrac{1}{2}) ,$$

$$S_+\beta=(\sqrt{\tfrac{2}{3}})(\tfrac{3}{2},-\tfrac{1}{2})+(\sqrt{3})^{-1}(\tfrac{1}{2},-\tfrac{1}{2}) ,$$

the matrix describing these splittings (in the basis $S_+\alpha$, $S_-\alpha$, $S_0\beta$) is

$$\begin{pmatrix} \Delta_1'+\frac{1}{2}a & 0 & 0 \\ 0 & \Delta_1'-\frac{2}{3}b-\frac{1}{6}a & (\sqrt{\frac{2}{3}})(b-\frac{1}{2}a) \\ 0 & (\sqrt{\frac{2}{3}})(b-\frac{1}{2}a) & -\frac{1}{3}(b+a) \end{pmatrix} .$$

By adding the constant $\frac{1}{3}(a+b)$ to the diagonal elements, this matrix becomes identical to Pikus's matrix if one makes the identifications

$$\Delta_1=\Delta_1'+\tfrac{1}{2}a, \qquad a=2(\Delta_2-\Delta_3) ,$$

$$\Delta_2=\tfrac{1}{3}(a+b), \qquad b=\Delta_2+2\Delta_3 ,$$

$$\Delta_3=\tfrac{1}{3}(b-\tfrac{1}{2}a), \qquad \Delta_1'=\Delta_1-\Delta_2+\Delta_3 .$$

The operator H_{v-p} which describes the interaction between the valence bands due to strain can be determined from symmetry considerations by combining the strain tensor ϵ_{ij} with the angular momentum operators J and σ, as described by Pikus.[24] For zinc-blende symmetry,

$$H^{\mathrm{ZB}}_{v-p}=C_1(\epsilon_{xx}+\epsilon_{yy}+\epsilon_{zz})+C_2(J_x^2\epsilon_{xx}+J_y^2\epsilon_{yy}+J_z^2\epsilon_{zz})$$
$$+C_3([J_yJ_z]\epsilon_{yz}+[J_xJ_z]\epsilon_{xz}+[J_xJ_y]\epsilon_{xy}) ,$$

where

$$[AB]=\tfrac{1}{2}(AB+BA) .$$

For wurtzite symmetry, Pikus obtained

$$H^{w}_{v-p}=(C_1+C_3J_z^2)\epsilon_{zz}+(C_2+C_4J_z^2)(\epsilon_{xx}+\epsilon_{yy})$$
$$+C_5(J_-^2\epsilon_++J_+^2\epsilon_-)+C_6([J_zJ_+]\epsilon_{-z}$$
$$+[J_zJ_-]\epsilon_{+z}) ,$$

where

$$\epsilon_\pm=\epsilon_{xx}-\epsilon_{yy}\pm 2i\epsilon_{xy} , \quad \epsilon_{\pm z}=\epsilon_{xz}\pm i\epsilon_{yz} .$$

These operators then describe the mixing of the p-like valence bands due to crystalline strain in terms of material-dependent parameters.

The operator H_c represents the conduction-band energy. Because of the Γ_1 symmetry of the conduction band, the operator has the form

$$H_c^{\mathrm{ZB}}=E_c+d_1(\epsilon_{xx}+\epsilon_{yy}+\epsilon_{zz}) ,$$

$$H_c^{w}=E_c+d_1\epsilon_{zz}+d_2(\epsilon_{xx}+\epsilon_{yy}) .$$

The exciton part of the Hamiltonian can be written

$$H_{\mathrm{exciton}}=\mathrm{BE}+\tfrac{1}{2}j\,\sigma_h\cdot\sigma_c ,$$

where BE is the customary exciton binding energy (exclusive of exchange). The last term was suggested by Akimoto and Hasegawa[12] to describe the crystalline exchange interaction. The exchange constant j will be treated here as an adjustable parameter, although a formalism for calculating j from known band properties has been developed by Rohner.[25] Both BE and j will be assumed to be strain independent. The operator σ_h operates on valence-*hole* spin functions, not on valence-*electron* spin functions. Writing the valence-*electron* wave function as

$$\psi_v=A\alpha+B\beta ,$$

the corresponding *hole* wave function must be orthogonal to ψ_v, and thus must have the form

$$\Phi_h=B^*\alpha-A^*\beta=K\sigma_y\Psi_v ,$$

where K is the complex conjugation operator, and where $K\sigma_y$ is Wigner's time-reversal operator for a one-electron system. Consequently, the matrix $\frac{1}{2}j\sigma_h\cdot\sigma_c$ with the valence-*hole*–conduction-electron basis, has the form

$$\left(\begin{array}{cccc} \alpha_h\alpha_c & \alpha_h\beta_c & \beta_h\alpha_c & \beta_h\beta_c \\ \frac{1}{2}j & 0 & 0 & 0 \\ 0 & -\frac{1}{2}j & j & 0 \\ 0 & j & -\frac{1}{2}j & 0 \\ 0 & 0 & 0 & \frac{1}{2}j \end{array}\right) ,$$

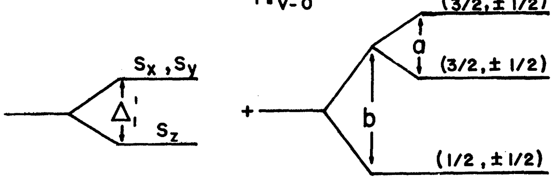

FIG. 15. Effect of the wurtzite crystal-field and spin-orbit Hamiltonian $H^{W}_{v\text{-}0}$ on the valence band.

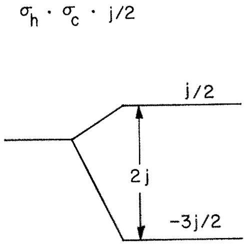

FIG. 16. Additional effect of the spin-exchange parameter j on the exciton levels.

while with the valence-*electron*-conduction-electron basis it has the form

$$\left(\begin{array}{cccc} \alpha_v\alpha_c & \alpha_v\beta_c & \beta_v\alpha_c & \beta_v\beta_c \\ -\frac{1}{2}j & 0 & 0 & -j \\ 0 & \frac{1}{2}j & 0 & 0 \\ 0 & 0 & \frac{1}{2}j & 0 \\ -j & 0 & 0 & -\frac{1}{2}j \end{array}\right).$$

In either representation, there are three eigenvalues $\frac{1}{2}j$ for the triplet spin states and one eigenvalue $-\frac{3}{2}j$ for the singlet spin state (see Fig. 16).

Combining all of these operators and dropping constant energies which equally effect all valence bands, we obtain the Hamiltonians

$$H^{\mathrm{ZB}} = \Delta J \cdot \sigma_v + C_1(\epsilon_{xx} + \epsilon_{yy} + \epsilon_{zz}) + C_2(J_x^2\epsilon_{xx} + J_y^2\epsilon_{yy} + J_z^2\epsilon_{zz}) + C_3([J_yJ_z]\epsilon_{yz} + [J_xJ_z]\epsilon_{xz} + [J_xJ_y]\epsilon_{xy}) + \tfrac{1}{2}j\,\sigma_h\cdot\sigma_c ,$$

$$H^w = \Delta_1 J_z^2 + \Delta_2 J_z\sigma_{zv} + \Delta_3(\sigma_{+v}J_- + \sigma_{-v}J_+) + (C_1 + C_3J_z^2)\epsilon_{zz} + (C_2 + C_4J_z^2)(\epsilon_{xx} + \epsilon_{yy}) + C_5(J_-^2\epsilon_+ + J_+^2\epsilon_-) + C_6([J_zJ_+]\epsilon_{-z} + [J_zJ_-]\epsilon_{+z}) + \tfrac{1}{2}j\,\sigma_h\circ\sigma_c ,$$

where the special symbols have been defined earlier.

A general wave function can then be written

$$\Psi = a_1(S_+\alpha\alpha) + a_2(S_-\alpha\alpha) + a_3(S_0\beta\alpha) + a_4(S_+\beta\beta) + a_5(S_-\beta\beta) + a_6(S_0\alpha\beta) + a_7(S_+\alpha\beta) + a_8(S_-\alpha\beta) + a_9(S_0\beta\beta) + a_{10}(S_+\beta\alpha) + a_{11}(S_-\beta\alpha) + a_{12}(S_0\alpha\alpha) ,$$

where the first spin is that of the (missing) valence *electron* and the second is that of the conduction electron. The resulting Hamiltonian matrices are given in Table I. It can be seen from the table that when the strain tensor is diagonal, the matrices split up into two 6×6 matrices. In the case of wurtzite symmetry, the first matrix describes the Γ_5 excitons, while the second describes the Γ_6, $\Gamma_{1,2}$ excitons. Diagonalization of these matrices then results in 12 exciton energies and 12 exciton wave functions. From these wave functions, one can calculate relative matrix elements for allowed optical transitions, $\langle 0|\xi\circ\nabla|\Psi\rangle$, where ξ gives the polarization of the light, and

TABLE I. Exciton matrix for Γ point.

	$S_+\alpha\alpha$	$S_-\alpha\alpha$	$S_0\beta\alpha$	$S_+\beta\beta$	$S_-\beta\beta$	$S_0\alpha\beta$	$S_+\alpha\beta$	$S_-\alpha\beta$	$S_0\beta\beta$	$S_+\beta\alpha$	$S_-\beta\alpha$	$S_0\alpha\alpha$
$S_+\alpha\alpha$	Λ_{1-}	δ_3	0	$-j$	0	0	0	0	0	0	0	δ_4
$S_-\alpha\alpha$	δ_3^*	Λ_{2-}	$\sqrt{2}\Delta_3$	0	$-j$	0	0	0	0	0	0	$-\delta_4^*$
$S_0\beta\alpha$	0	$\sqrt{2}\Delta_3$	Λ_{3+}	0	0	0	0		0	δ_4^*	$-\delta_4$	0
$S_+\beta\beta$	$-j$	0	0	Λ_{2-}	δ_3	$\sqrt{2}\Delta_3$	0	0	δ_4	0	0	0
$S_-\beta\beta$	0	$-j$	0	δ_3^*	Λ_{1-}	0	0	0	$-\delta_4^*$	0	0	0
$S_0\alpha\beta$	0	0	0	$\sqrt{2}\Delta_3$	0	Λ_{3+}	δ_4^*	$-\delta_4$	0	0	0	0
$S_+\alpha\beta$	0	0	0	0	0	δ_4	Λ_{1+}	δ_3	0	0	0	0
$S_-\alpha\beta$	0	0	0	0	0	$-\delta_4^*$	δ_3^*	Λ_2	$\sqrt{2}\Delta_3$	0	0	0
$S_0\beta\beta$	0	0	0	δ_4^*	$-\delta_4$	0	0	$\sqrt{2}\Delta_3$	Λ_{3-}	0	0	$-j$
$S_+\beta\alpha$	0	0	δ_4	0	0	0	0	0	0	Λ_{2-}	δ_3	$\sqrt{2}\Delta_3$
$S_-\beta\alpha$	0	0	$-\delta_4^*$	0	0	0	0	0	0	δ_3^*	Λ_{1+}	0
$S_0\alpha\alpha$	δ_4^*	$-\delta_4$	0	0	0	0	0	0	$-j$	$\sqrt{2}\Delta_3$	0	Λ_{3-}

Substitute for

Zinc blende	Wurzite
$\Lambda_{1\pm} = \Delta + \delta_1 + \delta_2 \pm \frac{1}{2}j$	$\Lambda_{1\pm} = \Delta_1 + \Delta_2 + \delta_1 + \delta_2 \pm \frac{1}{2}j$
$\Lambda_{2\pm} = -\Delta + \delta_1 + \delta_2 \pm \frac{1}{2}j$	$\Lambda_{2\pm} = \Delta_1 - \Delta_2 + \delta_1 + \delta_2 \pm \frac{1}{2}j$
$\Lambda_{3\pm} = \delta_5 + \delta_2 \pm \frac{1}{2}j$	$\Lambda_{3\pm} = \delta_1 \pm \frac{1}{2}j$
$\Delta_3 = \Delta$	$\delta_1 = C_1\epsilon_{zz} + C_2(\epsilon_{xx} + \epsilon_{yy})$
$\delta_1 = C_2\epsilon_{zz}$	$\delta_2 = C_3\epsilon_{zz} + C_4(\epsilon_{xx} + \epsilon_{yy})$
$\delta_2 = C_1(\epsilon_{xx} + \epsilon_{yy} + \epsilon_{zz}) + \frac{1}{2}C_2(\epsilon_{xx} + \epsilon_{yy})$	$\delta_3 = C_5(\epsilon_{xx} - \epsilon_{yy} - 2i\epsilon_{xy})$
$\delta_3 = \frac{1}{2}C_2(\epsilon_{xx} - \epsilon_{yy}) - \frac{1}{2}iC_3\epsilon_{xy}$	$\delta_4 = \frac{1}{2}C_6(\epsilon_{xz} - i\epsilon_{yz})$
$\delta_4 = C_3(\epsilon_{xz} - i\epsilon_{yz})/2\sqrt{2}$	
$\delta_5 = \frac{1}{2}C_2(\epsilon_{xx} + \epsilon_{yy})$	

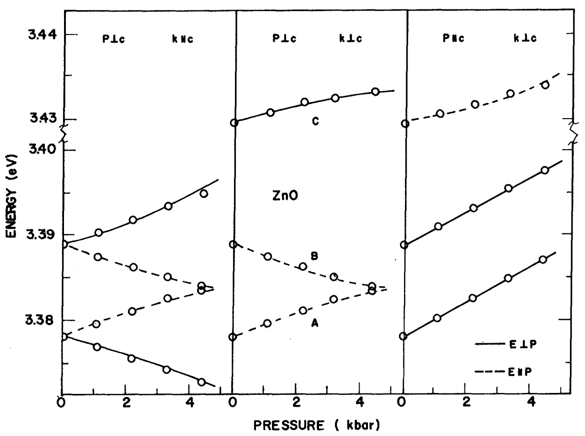

FIG. 17. Energy dependence of ZnO excitons on stress. Results of several measurements are averaged and adjusted to proper exciton position (solid lines $\vec{E}\perp\vec{P}$; dashed lines $\vec{E}\parallel\vec{P}$). Points represent calculated values using parameters of Tables II and III.

where $|0\rangle$ corresponds to a filled valence band and empty conduction band. Transition probabilities are thus proportional to

$$x \text{ direction: } \tfrac{1}{2}(-a_1+a_2-a_4+a_5)^2 ,$$

$$y \text{ direction: } \tfrac{1}{2}(a_1+a_2+a_3+a_4)^2 ,$$

$$z \text{ direction: } (a_9+a_{12})^2 .$$

V. DISCUSSION AND CONCLUSIONS

Having developed the appropriate theoretical expressions in Sec. IV, we can now do a least-squares fit to the experimental curves according to a modified method of steepest descent.[26] The experimental curves used for this fit (Figs. 17–19) were derived from averages of five to six such sets of measurements as illustrated in Figs. 4, 6, and 8. The averaged curves have been translated along the energy scale, in order to match the zero-pressure values of these curves with the exact position of the respective excitons as determined by absorption measurements. This adjustment implies that the energy difference, e.g., between a reflection minimum and the absorption maximum is pressure independent, which is a reasonable approximation derived from an inspection of the reflection curves at different pressures.

The elastic constants and zero-pressure exciton levels used in the calculations are listed in Table II. The fit is done simultaneously for all curves pertaining to $\vec{P}\parallel c$ and $\vec{P}\perp c$ of a given wurtzite compound. Additional constraints were introduced to ensure that the observed polariza-

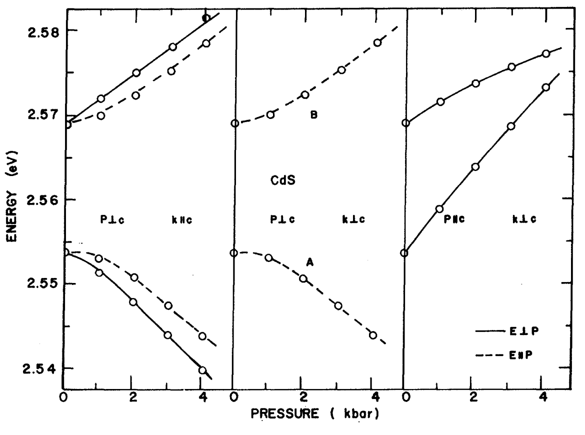

FIG. 18. Energy dependence of CdS excitons on stress, analogous to Fig. 17.

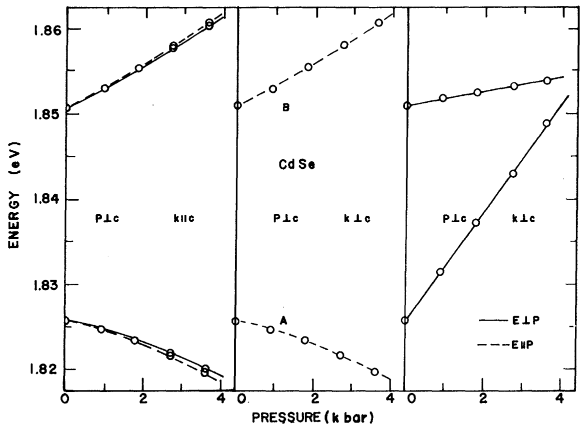

FIG. 19. Energy dependence of CdSe excitons on stress, analogous to Fig. 17.

TABLE II. Exciton energies (A, B, C) and elastic compliance constants (S) used in the theory for comparison with the experimental data. Exciton energies in eV; elastic compliance constants in 10^{-6} bar^{-1}; exciton energies for $n=1$ states from own measurements. Elastic constant ZnO, cf. T. B. Bateman, J. Appl. Phys. 33, 3309 (1962). S_{44} and S_{66} were corrected according to C_{44} and C_{66}. Other crystals, cf. Berlincourt *et al.*, Phys. Rev. 129, 1009 (1963).

	ZnO	CdS	CdSe	ZnS	ZnSe
A	3.378	2.553	1.826	3.804	2.80
B	3.389	2.569	1.851	3.869	3.21
C	3.429	2.630	2.283	⋯	⋯
S_{11}	0.7858	2.069	2.338	1.786	2.26
S_{12}	−0 3432	−0.999	−1.122	−0.685	−0.85
S_{13}	−0.2206	−0.581	−0.572	⋯	⋯
S_{33}	0.6940	1.697	1.735	⋯	⋯
S_{44}	2.357	6.649	7.595	2.148	2.27
S_{66}	2.258	6.136	6.920	⋯	⋯

tions were matched correctly and that increases (or decreases, respectively) of intensities as a function of pressure were also qualitatively reproduced by the resulting set of parameters.[27]

For wurtzite crystals, nine parameters were simultaneously adjusted to give the best fit. They reflect the crystal-field and spin-orbit splittings, the strength of the spin exchange, and the deformation potentials of the bands at the Γ point. Though this seems to be a high number of adjustable parameters, one should remember that, e.g., in the case of ZnO we fit a total of eight functions of pressure simultaneously, together with the above-mentioned additional constraints on polarization and intensity.

In order to evaluate the merit of the parameters determined by this procedure, we shall compare in detail the resulting theoretical intensities with those observed experimentally.

A. Hexagonal Crystals

In Figs. 17–19, one may compare the experimentally determined changes of the exciton levels as a function of uniaxial stress (solid lines) and the theoretical best-fit values (circles). The parameters thus determined are listed in Table III.

The deformation potentials, C_i given in eV, are probably accurate to within 20%. The different sign of C_5 for CdSe in comparison to C_5 in CdS and ZnO results from the reversal of polarization for the $\vec{E} \perp \vec{P}$ and $\vec{E} \parallel \vec{P}$ branches in CdSe ($\vec{P} \perp C, \vec{k} \parallel c$) in contrast to the other two compounds.

The deformation potential C_6, included in Table III, is not effective in either of the stress directions $\vec{P} \perp c$ or $\vec{P} \parallel c$ for which the fit was made. It is, however, effective when, e.g., the direction of stress forms an angle of 45° with the c axis. Measurements of the exciton levels under stress in this orientation have been made and are shown as solid lines in Fig. 20. The theory was fitted with C_6 as an adjustable parameter and with the Δ_{1-3}, j and C_{1-5} values as determined from the previous fit. The agreement obtainable may also be interpreted as a test of the formerly derived set of nine parameters. The agreement for ZnO is very good, that for CdS and CdSe is not as good, which in part may be due to the fact that in these latter compounds the pressure dependence of the C exciton was not included in the $\vec{P} \perp c$ and $\vec{P} \parallel c$ fits. Because of the relatively wide width of the C exciton reflection structure in CdS and CdSe, we were unable to reliably determine its pressure dependence and it was, therefore, not included.

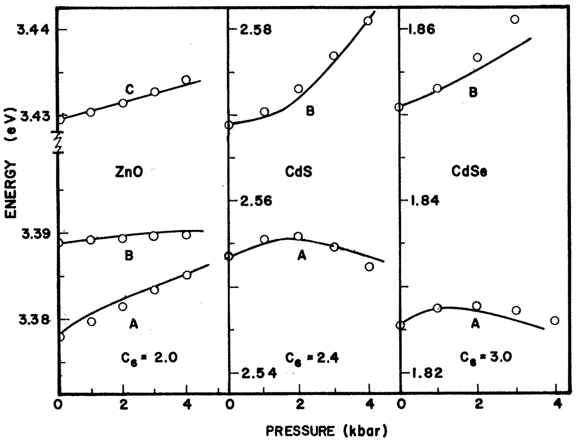

FIG. 20. Energy dependence of excitons in ZnO, CdS, and CdSe for $\vec{P}$ at 45° to c axis are shown as solid lines. Points represent calculated values, using the same parameters as in calculations to Figs. 17–19 and additionally the indicated C_6 values.

TABLE III. Deformation potentials (C), spin-exchange (j), and crystal-field and spin-orbit (Δ) parameters resulting from fit for data of hexagonal crystals. For comparison j^*, the calculated exchange parameter. Units of Δ's, j and j^* are meV. Units of C's are eV. j^* calculated by Rohner (Ref. 25).

	ZnO	CdS	CdSe
Δ_1	36.3	28.4	68.8
Δ_2	1.9	20.9	138.0
Δ_3	7.4	20.7	150.7
j	5.6	2.5	0.4
j^*	5.9	2.3	0.8
C_1	− 3.8	− 2.8	− 0.76
C_2	− 3.8	− 4.5	− 3.7
C_3	− 0.8	− 1.3	− 4.0
C_4	1.4	2.9	2.2
C_5	− 1.2	− 1.5	1.2
(C_6)	2.0	2.4	3.0

The values of the exchange parameter j (listed in meV) show an expected trend, namely, that their values are related to the radii of the excitons. The value of j is smallest for CdSe, which has the largest exciton radius; it is increased for CdS and largest for ZnO, which has the smallest exciton radius of these three compounds. In general, the consequences of the exchange effect is that the observed energy separations between the A, B, and C excitons are no longer determined only by the splitting of the valence bands; and the less so, the larger j is.

Further, as Dos, Haug, and Rohner[28] pointed out on the basis of their perturbation calculation, the spin exchange influences most the 1s and less the higher s states of the exciton spectrum. This has the effect that for larger j values the exciton spectrum is no longer hydrogenlike. This points out the danger of calculating an exciton binding energy from the separation of the observed $n = 1$ and $n = 2$ states with a hydrogenlike formulation. In fact, this has been frequently done[15, 29, 30] because separation between the $n = 2$ and $n = 3$ states is subject to a greater experimental uncertainty. Rohner[25] calculated the spin-exchange parameter and the shift of the 1s exciton level due to the exchange interaction by using the high-frequency dielectric constant and the effective mass of the exciton. The results of his calculations are included in Table III for a comparison. The 1s state is shifted, he concludes, by the amount of $2j$ towards higher energies in comparison with a true hydrogenlike series.

The Δ_1, Δ_2, and Δ_3 (given in meV in Table III) determine the crystal-field and spin-orbit parameters, and, consequently, the splitting of the upper valence band. The crystal-field parameter Δ_1' is given by

$$\Delta_1' = \Delta_1 - \Delta_2 + \Delta_3 .$$

The resulting spin-orbit parameter b and the trigonal spin-orbit parameter a are

$$a = 2(\Delta_2 - \Delta_3) \quad \text{and} \quad b = \Delta_2 + 3\Delta_3 .$$

In the quasicubic approximation Δ_3 is equal to Δ_2; that is, the trigonal parameter is zero.

In Table IV, we compare material constants derived from the present work with those resulting from the quasicubic model. The value of the trigonal spin-orbit parameter, or more meaningfully, the value of a/b, the ratio of the trigonal to the isotropic spin-orbit parameter, enables us to evaluate in principle the validity of the quasicubic model. The largest error, it seems, is introduced by its application to ZnO, where a is 66% of b. In ZnO, we remember the c'/a' lattice constant ratio deviates most from the ideal ratio for wurtzite compounds, less so in CdS and least in CdSe. Contrary to this expected sequence, we observe that the a/b ratio is smaller in CdS than in CdSe, 0.6% versus 5.8%, respectively. We should, however, emphasize that our fits to the experimental data for CdS and CdSe are not as well founded as for ZnO, owing to the lack of data on the stress dependence of the C exciton. Consequently, the C_i and Δ_i values for CdS and CdSe are less reliable than their counterparts for ZnO. The values of a and b, being composites of Δ_i, might carry a still larger error. In other words, we think that within the experimental accuracy and the reliability of the fitting procedure, both values might be near zero, i.e., the necessity for the application of the quasicubic model is in praxis fulfilled in CdS and CdSe.

The values of δ_{so} and Δ_{cf} are the customarily calculated spin-orbit and crystal-field parameters according to the quasicubic model, neglecting the exchange effect. They should be compared with b and Δ_1'.

In the framework of the quasicubic model, the experimentally observed energy separations of the A and B excitons E_{AB} and the separation between B and C E_{BC} are supposed to be equal to the energy separations between the first and second valence bands E_{12} and the second and third bands E_{23}, respectively. We added to Table IV the calculated values for E_{12} and E_{23} on the basis of the present work (see Fig. 21). While the agreement between exciton separation and valence-band separations is fairly good in CdSe and CdS, the combined effect of the trigonal spin-orbit parameter and the exchange effect shows a marked difference in ZnO comparing E_{AB} with E_{12}. It appears that the top two valence bands are very nearly degenerate, more so than the energy difference of the A and B excitons would suggest.

Using the parameters listed in Table III, we calculated the intensities of the excitons (in arbitrary units). In Table V such results are shown for the A and B excitons in ZnO and CdS with $\vec{P} \perp c$, $\vec{k} \parallel c$. We shall compare them with our experimental results, which, though not quantitative, allow a qualitative comparison, especially when one compares values derived from the same spectroscopic exposure, e.g., when one compares the relative strengths of the A and B excitons of a compound at a given pressure, direction of observation, and polarization.

Experimentally at atmospheric pressure (0 kbar) the A exciton in ZnO is very weak compared with the B exciton, while, in CdS, A and B excitons show reflection anomalies of similar magnitude. The calculated results of A/B (0.0012 for ZnO and 1.1 for CdS) predict this different intensity ratio; it probably even exaggerates the intensity difference between the A and B excitons in ZnO. This intensity ratio depends critically on j and the magnitude of j compared with the spin-orbit splitting, which is in accordance with the work of Onodera and Toyozawa for alkali halides.[31]

With increasing pressure (compare ZnO with Fig. 3), the high-energy component of the A exciton ($\vec{E} \parallel \vec{P}$) compared with the low-energy component of the B exciton ($\vec{E} \parallel \vec{P}$) increases in intensity up to the point where a reversal of the magnitudes occurred (solid line in Sec. 3 of Fig. 3) between 3.39 and 4.24 kbar and between 3.3 and 4.4 kbar in the calculation. For $\vec{E} \perp \vec{P}$ (dashed line in right-hand section of Fig. 3), the ratio A/B seems to show no pressure-dependent change; the calculated intensities are also relatively pressure independent. The results for CdS should be compared with Fig. 7. For $\vec{E} \parallel \vec{P}$ (solid line in

TABLE IV. Spin-orbit and crystal-field parameter, and energy separations of excitons and valence-band energies. All units are meV.

		ZnO	CdS	CdSe
Spin-orbit parameter	a	−11.0	− 0.4	− 25.4
	b	16.7	48.6	439.
	$-a/b$	0.66	0.006	0.058
	δ_{so} [a]	19	64.3	443
Crystal-field parameter	Δ_1'	41.8	28.2	81.5
	Δ_{cf}[a]	43	28.8	39
Exciton separations (expt)	E_{AB}	10.7	16	25.3
	E_{BC}	40.7	61	432
Valence band separations (calculated from Δ's)	E_{12}	0.87	16.0	25.5
	E_{23}	40.3	59.0	432

[a] Quasicubic values derived according to Hopfield (Ref. 4) using A, B, and C energies from Table II. In the quasicubic approximation $E_{AB}=E_{12}$ and $E_{BC}=E_{23}$.

Fig. 7), the ratio A/B has been calculated to increase with pressure – as observed – and similarly for ZnO. For $\vec{E}\perp\vec{P}$ (dashed line in Fig. 7), we noticed, however, for CdS a decrease of A/B with increasing pressure, which was not observed in ZnO. Again, the calculation is in agreement with this behavior. In ZnO, A/B decreases by roughly 25% between 0 and 4.4 kbar, whereas in CdS, A/B decreases by more than an order of magnitude in the same pressure interval.

It might be interjected here that a different interpretation of the ZnO exciton spectra has been suggested in the recent literature. In the present work, we followed Thomas's assignment of excitons A, B, and C. The energies of the respective absorption maxima (or reflection anomalies) are little disputed. Park *et al.*[29] argued that the absorption, assigned to the free A exciton by Thomas, is, in fact, due to a bound exciton. They consequently change Thomas's assignments of the B and C excitons. Although our experiments cannot be constructed to be a direct proof of Thomas's assignment because the calculations are based on his energy assignments, our results are, however, consistent with it and support it. In particular, the observed, surprisingly low intensity of the A exciton in comparison to the B exciton in ZnO (in contrast to ZnS, CdS, and CdSe) is well accounted for and should no longer be considered as supporting evidence of Park's assignment.

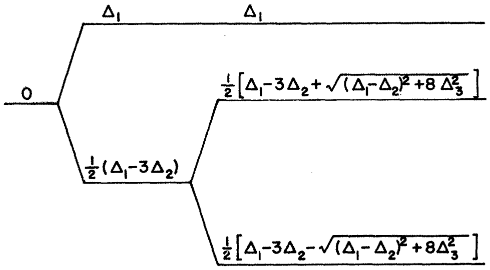

FIG. 21. Zero-pressure splitting of the valence bands in wurtzite II-VI compounds in terms of Δ_1, Δ_2 and Δ_3. The exact splittings of the excitons, including the spin exchange, cannot be represented by a closed algebraic form.

B. Cubic Crystals

For cubic crystals of II-VI compounds, the theory of Sec. IV also provides us with estimates of the change of exciton energies and intensities under uniaxial pressure. We calculated these values to match our experimental results of Figs. 11 and 12. We used as adjustable parameter the spin exchange j and the deformation potentials C_1 and C_2. It is assumed that the relation $C_3=2C_2$ is valid. The resulting parameter, which represents well the experimental curves, is shown in Table VI.

The spin-orbit parameter was not included in the fit because of the relative uncertainty of the experimental data for the broad structure of the B excitons. In the calculations, we used $\Delta(\text{ZnS}) = 70$ meV[20] and $\Delta(\text{ZnSe}) = 410$ meV.

The spin-exchange parameter j should have the value of about 4 meV in ZnS and 1 meV in ZnSe. These values agree with those of the hexagonal crystals in that the correspondence between exciton radius and spin-exchange parameter (the smaller the exciton radius the larger the spin exchange) holds for all investigated compounds. Rohner's calculations[25] yield spin-exchange values of 4.0

TABLE V. Calculated intensities for A and B excitons ($\vec{P}\perp c$, $\vec{k}\parallel c$). Units of intensity are arbitrary.

		$E\parallel P$			$E\perp P$		
	Pressure (kbar)	A	B	A/B	A	B	A/B
ZnO	0	0.0044	3.72	0.0012	0.0044	3.72	0.0012
	1.1	0.0074	3.76	0.0019	0.0043	3.71	0.0011
	2.2	0.0156	3.77	0.0041	0.0039	3.70	0.0011
	3.3	0.0665	3.75	0.0177	0.0036	3.69	0.0010
	4.4	3.36	0.470	7.15	0.0033	3.67	0.0009
CdS	0	1.57	1.45	1.1	1.57	1.45	1.1
	1.0	2.36	0.84	2.8	0.97	2.0	0.49
	2.0	2.90	0.44	6.6	0.64	2.3	0.29
	3.0	3.21	0.24	13.4	0.46	2.4	0.19
	4.0	3.40	0.14	24.1	0.34	2.5	0.14

and 1.25 for ZnS and ZnSe, respectively. His values for these cubic compounds are, however, less reliable than for the hexagonal compounds, because the values of the high-frequency dielectric constant had to be estimated and further, there are no reliable values available for the binding energy of excitons in cubic ZnS and ZnSe.

Figure 22 represents the calculated energy and intensity variations of excitons in cubic crystals for $\vec{P}\parallel[111]$. On the left-hand side of Fig. 22 is shown the energy dependence of the A exciton. The dashed curve represents the actual case of ZnSe (cf. right-hand side of Fig. 11), the dotted curve the actual case of ZnS (cf. right-hand side of Fig. 12). The solid line is added to illustrate the contribution of the spin exchange: It represents the case of ZnSe (Δ and c's taken from the actual ZnSe case) with a zero spin-exchange parameter. It illustrates in comparison with the dashed curve the shift of the zero-exciton position and the splitting of the lower quasi-pressure-independent branch into two completely polarized components. The origin of the dotted curves is still further displaced at atmospheric pressure from the origin of the solid lines and the splitting is wider because ZnS has a four times larger exchange value. The different slopes, especially that of the upper $\vec{E}\perp\vec{P}$ branch of the dotted lines compared with the solid one, are due to the different deformation potentials and elastic constants for this case of ZnS.

TABLE VI. Deformation potentials (C) and spin-exchange parameter (j) resulting from fit to data of cubic crystals. For comparison j^*, the calculated exchange parameter. Units of j and j^* in meV, C_i in eV.

	ZnS	ZnSe
j	4	1
j^{*a}	4.0	1.25
C_1	2.5	3.0
C_2	2.25	3.6

[a] j^* calculated by Rohner (Ref. 25).

The calculated intensities, displayed at the right-hand part of Fig. 22, agree similarly with the observations: The influence of the spin exchange is to increase the intensity of the lower $\vec{E}\perp\vec{P}$ branch at higher pressure. Furthermore, the larger the spin exchange, the slower is the rise of intensity of this branch, and the higher the pressure at which it finally reaches a pressure-independent value. The intensity calculations thus confirm well the observations described above in Sec. III. Additional measurements on ZnSe with $\vec{P}\parallel[100]$ were also satisfactorily explained with the relevant parameters of Table VI.

It should be emphasized that the lower $\vec{E}\perp\vec{P}$ branch observed at higher pressure is not split off from the Γ_5 exciton at atmospheric pressure. It is actually a normally forbidden component of the A exciton, already separated at atmospheric pressure from the Γ_5 position due to the contribution of the exchange. With increasing pressure, however, it gains intensity and thus becomes observable. This is in contrast to the splitting of the A and B excitons in hexagonal crystals, where the splitting corresponding to the $\vec{E}\perp\vec{P}$ upper branch, and the $\vec{E}\parallel\vec{P}$ branch of cubic crystals is affected by the crystal field and where then, if $\vec{P}\perp c$ and $\vec{k}\parallel c$, a further splitting of the Γ_5 components of the A and B excitons is observed.

It might be injected here that it is not clear that the lower-energy component with $\vec{E}\perp\vec{P}$ is apparently different in energy from the $\vec{E}\parallel\vec{P}$ component. We traced a characteristic point of the reflection structure – the minimum – which with identical oscillator resonance frequency will be displaced toward lower energies for a smaller oscillator

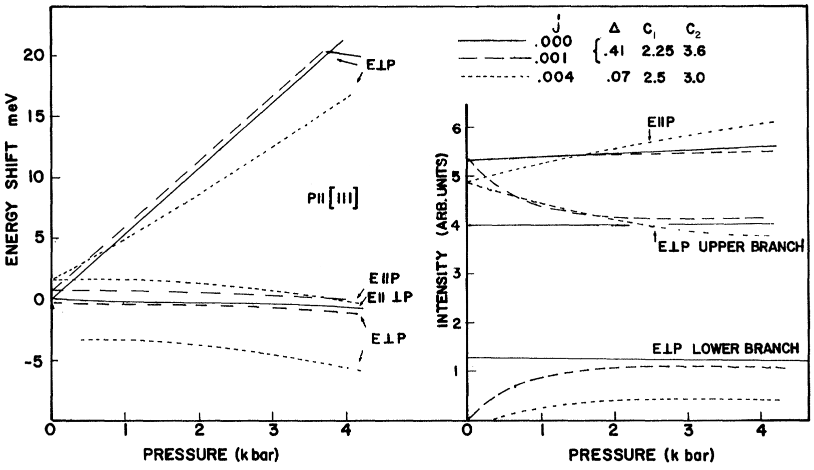

FIG. 22. Left part represents the calculated stress-induced splitting and shifts of the *A* exciton in ZnS (dotted line) and for ZnSe (dashed line). The solid line represents ZnSe, but with zero spin-exchange parameter. The right-hand side represents the stress-induced intensity variation of the respective components.

frequency. This point can only truly be decided by quantitative intensity measurements and subsequent Kramers-Kronig analysis of the data. The lack of a Kramers-Kronig analysis certainly will enter as an uncertainty in the final determination of parameters – as it does in the work of the previous workers.[5-9] We estimate, however, that it cannot account for the large observed displacements. Furthermore, (i) the pressure-induced change of the intensity is in agreement with our theoretical interpretation, and (ii) comparing compounds with different exchange constants, the predicted trend is also observable, i.e., the smaller the exchange j, (a) the smaller is the energy difference between the lower $\vec{E} \parallel \vec{P}$ and $\vec{E} \perp \vec{P}$ branch, (b) the stronger is the lower $\vec{E} \perp \vec{P}$ branch with respect to the upper $\vec{E} \perp \vec{P}$ branch, and (c) the earlier, with increasing pressure, will the lower $\vec{E} \perp \vec{P}$ gain intensity and saturate. It thus also appears to be reasonable that in CdTe, which would have a still smaller j value then ZnSe, the splitting of the lower branches had not been seen by Thomas.[5]

We thus conclude that the theory of Sec. IV adequately describes our observations, and that the resulting parameters not only describe the energy dependence of the excitons upon stress, but also account qualitatively for the observed stress-induced intensity changes.

VI. SUMMARY

The main purpose of this paper was to draw attention to the effects of the spin exchange in Wannier-type excitons in compounds with p-like valence bands. The theory, outlined in Sec. IV, enabled us to deduce the magnitude of the spin-exchange parameter from our experimental data originating from measurements of the shift of exciton levels under uniaxial externally applied stress. It became apparent that this effect is larger than expected and increasingly more important the smaller the exciton radius in a compound. The magnitude of the exchange parameters is in good agreement with recent first-principles calculations by Rohner. It also became obvious that, at least when the exchange parameter is large as in ZnO and ZnS, the energy separation between *A*, *B*, (and *C* in hexagonal crystals) excitons is not equal to the energy separations of the doubly or triply split valence bands. Similarly, the spin-exchange parameter will influence the energy position of the *s* states of Wannier excitons and thus binding energies should not be deduced from 1*s* and 2*s* states by assuming a hydrogenlike series for materials with a large exchange parameter.

The magnitude of the crystal-field parameter, the isotropic spin-orbit parameter, and the trigonal spin-orbit parameter, which combined cause the splitting of the valence bands, were deduced by the same set of experiments (Table III). The comparison to the often used quasicubic model for hexagonal compounds was made in Table IV.

Finally, this work also resulted in the determination of the deformation potentials given in Tables III and VI. The inclusion of the exchange parameter in the evaluation of the stress-induced shifts of the exciton levels proved to be necessary for the qualitative explanation of the results and for a correct deduction of the deformation-potential values. The stress-induced intensity variations of the exciton reflection anomalies are well represented by our description as are also the relative intensities of the excitons in different compounds at atmospheric pressure.

ACKNOWLEDGMENTS

We would like to thank Dr. P. Rohner for communicating the results of his calculations to us prior to publication. Further, we thank D. E. Johnson for the preparation of the samples.

[*] Present address: National Institute for Research on Inorganic Materials 29-3, 2-Chome, Honkomagome, Bunkyo-ku, Tokyo 113, Japan.

[†] Present address: Department of Applied Physics, University of Tokyo, Tokyo, Japan.

[1] R. S. Knox, *Theory of Excitons* (Academic, New York, 1963).

[2] D. C. Reynolds, C. W. Litton, and T. C. Collins, Phys. Status Solidi 9, 645 (1965).

[3] J. J. Hopfield, J. Phys. Chem. Solids 15, 97 (1960).

[4] S. L. Adler, Phys. Rev. 126, 118 (1962); V. V. Sobolev, Fiz. Tverd. Tela 6, 906 (1964)[Soviet Phys. Solid State 6, 697 (1964)].

[5] D. G. Thomas, J. Appl. Phys. Suppl. 32, 2298 (1961).

[6] L. T. Chadderton, R. B. Parsons, W. Wardzinski, and A. D. Yoffe, J. Phys. Chem. Solids 23, 418 (1962); M. Grynberg, *Proceedings of the International Conference on the Physics of Semiconductors, Paris*, 1964 (Dunod, Paris, 1964), p. 135; Phys. Status Solidi 27, 255 (1969).

[7] A. A. Kaplyanskii and L. G. Suslina, Fiz. Tverd. Tela 7, 2327 (1965) [Soviet Phys. Solid State 7, 1881 (1966)].

[8] J. E. Rowe, M. Cardona, and F. H. Pollak, *Proceedings of the International Conference on II-VI Semiconducting Compounds, Providence, Rhode Island*, 1967 (Benjamin, New York, 1967), p. 112.

[9] J. E. Rowe, M. Cardona, and F. H. Pollak, Solid State Commun. 6, 239 (1968).

[10] W. H. Kleiner and L. M. Roth, Phys. Rev. Letters 2, 334 (1959).

[11] T. Koda and D. W. Langer, Phys. Rev. Letters 20, 50 (1968).

[12] O. Akimoto and H. Hasegawa, Phys. Rev. Letters 20, 916 (1968); Bussei 9, 134 (1968).

[13] T. Koda, D. W. Langer, and R. N. Euwema, *Proceedings of the International Conference on the Physics of Semiconductors, Moscow*, 1968 (Nauka, Leningrad, 1968), p. 242; K. Era, R. N. Euwema, and D. W. Langer, Bull. Am. Phys. Soc. 13, 1476 (1968).

[14] J. E. Rowe, F. H. Pollak, and M. Cardona, Phys. Rev. Letters 22, 933 (1969).

[15] A. Ebina and T. Takahashi, J. Appl. Phys. 38, 3079 (1967); G. V. Anan'eva, K. K. Dubenskii, A. I. Ryskin, and G. I. Khiliko, Fiz. Tverd. Tela 10, 1800 (1968) [Soviet Phys. Solid State 10, 1417 (1968)].

[16] D. G. Thomas, J. Phys. Chem. Solids 15, 86 (1960).

[17] D. G. Thomas and J. J. Hopfield, Phys. Rev. 116, 573 (1959).

[18] J. O. Dimmock and R. G. Wheeler, J. Appl. Phys. 32, 2271 (1961); R. G. Wheeler and J. O. Dimmock, Phys. Rev. 125, 1805 (1962).

[19] G. E. Hite, D. T. F. Marple, M. Aven, and B. Segall, Phys. Rev. 156, 850 (1967).

[20] J. L. Birman, H. Samelson, and A. Lempicki, GT&T. Res. Develop. J. 1, 2 (1961).

[21] Marvin L. Cohen, *Proceedings of the International Conference on II-VI Semiconducting Compounds, Providence, Rhode Island*, 1967 (Benjamin, New York, 1967), p. 462.

[22] Frank Herman *et al.*, Ref. 21, p. 503; R. N. Euwema, T. C. Collins, P. G. Shankland, and J. S. DeWitt, Phys. Ref. 162, 710 (1967); D. J. Stukel, R. N. Euwema, T. C. Collins, F. Herman, and R. L. Kortum, *ibid.* 179, 740 (1969).

[23] J. Treusch, P. Eckelt and O. Madelund, Ref. 21, p. 588; U. Rössler, Phys. Rev. 184, 733 (1969).

[24] G. E. Pikus, Fiz. Tverd. Tela 6, 324 (1964) [Soviet Phys. Solid State 6, 261 (1964)].

[25] P. Rohner, Phys. Rev. (to be published).

[26] R. Fletcher and M. J. D. Powell, Computer J. 6, 163 (1963).

[27] Results differ slightly from those of Ref. 13. Improved fit has been achieved by fitting all $\vec{P}\perp c$ and $\vec{P}\parallel c$ experiments simultaneously.

[28] K. Dos, A. Haug, and P. Rohner, Phys. Status Solidi 30, 619 (1968).

[29] Y. S. Park, C. W. Litton, T. C. Collins, and D. C. Reynolds, Phys. Rev. 143, 512 (1966).

[30] W. Y. Liang and A. D. Yoffe, Phys. Rev. Letters 20, 59 (1968).

[31] Y. Onodera and Y. Toyozawa, J. Phys. Soc. Japan 22, 833 (1967).

PHYSICAL REVIEW B VOLUME 2, NUMBER 10 15 NOVEMBER 1970

Excitons, Plasmons, and Polaritons in Insulating Crystals*

Manfred Lang
Siemens AG, Research Laboratories, Munich, Germany

(Received 30 March 1970)

In this paper, a quantum-mechanical model of interacting radiation and nonmetallic matter is used to study the connection between excitons, plasmons, and polaritons. An explicit description of polaritons as mixed particles consisting of photons and matter oscillators is given, and it is shown that polariton states form a suitable basis for calculations of nonlinear optical effects in crystals. Plasmon-photon interactions, in addition, are shown to occur in the crystal.

INTRODUCTION

Since intense laser-light sources became available, nonlinear optical effects[1] such as Brillouin and Raman scattering, two-photon absorption, and harmonic generation have been observed, and the interaction between strong electromagnetic waves